

Mechanisms and advanced photothermal modelling of laser-induced shape transformations of colloidal gold nanorods by nanosecond laser pulses

Yehia Mansour, Yann Battie,* Aotmane En Naciri, and Nouari Chaoui

We propose an advanced photothermal model based on modified Takami model (MTM) to explain the mechanisms of shape changes of colloidal gold nanorods (NRs) induced by nanosecond laser pulses. This model takes into account the orientation of NR, the radiative and convective losses, and the phase transitions of NRs. It was applied to the determination of the evolution of temperature and the shape and size transformations of NRs during the laser exposure. A series of measurements arising from the interaction between Au NRs and nanosecond laser pulse were analyzed by TEM measurements and MTM model. We have demonstrated that the fragmentation and reshaping processes govern the nanoparticle (NP) shape. At high laser fluence, the complete fragmentation leads to a population of nearly spherical NPs while at moderate laser fluence, the partial fragmentation and reshaping processes generates a bimodal distribution. At low laser fluence, uncommon ϕ -shape NPs were produced as a result of the competition of cooling and reshaping processes. We also demonstrated that it is possible by MTM model to determine the laser fluence required to suppress some specific NRs shapes and to predict the NP size and shape distributions obtained after the laser exposure.

Introduction

Gold nanoparticles (NPs) exhibit strong plasmon resonance, induced by the collective oscillation of their conduction electrons, whose characteristics depend on the NP size and shape. The interaction of colloidal Au NPs with a pulsed laser beam attracts a growing interest, motivated by the opportunity to tailor the morphology of NPs¹⁻⁷ and to use them as efficient nanoheaters⁸ for the nanophotothermolysis of malignant tissues⁹⁻¹².

As reported by several authors^{2,13-16}, the exposure of Au colloids to a pulsed laser beam could lead to the reshaping and the fragmentation of NPs. This change of the NP morphology involves two different mechanisms depending on the pulse width¹⁷⁻¹⁸: The Coulomb explosion¹⁹ and the photothermal evaporation²⁰⁻²¹. Both of them are governed by the electron dynamics and various relaxation processes²²⁻²³. In femtosecond regime, the photo-excited electrons cannot transfer their energy to the NP lattice during the laser pulse. Indeed, pump-probe measurements revealed that the electron-phonon relaxation time is on the order of few picoseconds²². Thus, the NP size reduction in femtosecond pulse regime is due to the Coulomb explosion induced by the ejection of photo-excited electrons and the strong charge repulsion in ionized NPs. On the contrary, in nanosecond pulse regime, the NP size reduction is induced by the energy deposited into the NP lattice resulting in the heating of NPs to the boiling point of Au²¹. Whereas, both mechanisms have been intensively compared¹⁷⁻¹⁸, the modeling of photothermal mechanism is still an important issue to control the morphology of NPs exposed to ns-laser pulses.

According to the photothermal mechanism, Takami *et al.*²¹ have developed a model to correlate the phase transitions of NPs to the absorbed energy. They consider that the energy absorbed by a NP irradiated by a single ns-laser pulse serves to heat the NP and, if it is sufficient, to melt and vaporize it. This model is

applied on spherical NPs to qualitatively explain the relationship between the maximum diameter of spherical Au NPs and the laser fluence²¹. However, the Takami model (TM) considers the NP as an isolated system and neglects the energy transfer from the NP to the surrounding medium. This hypothesis is only valid if the laser pulse width is shorter than the time scale of energy losses. However, this latter case occurs during a ns-pulse exposure. In addition, Inasawa *et al.*²⁴ have shown that the NP reshaping and fragmentation can be observed below the fluence threshold calculated by the TM. This discrepancy could be attributed to surface partial melting and vaporization of NPs which are not taken into account in the TM. Link *et al.*² have applied the TM to non-spherical NPs such as nanorods (NRs). The absorption cross section of NRs, which is a key parameter for the TM, is estimated from absorption spectroscopy measurements performed on Au colloids. However, the value of the absorption cross section estimated by Link *et al.*² does not take into account scattering losses and the size and shape distributions of NPs. As a consequence, the fluence thresholds which induce phase transition of NPs, are misestimated. Despite that much effort has been devoted to model and elucidate the mechanisms behind the photothermal reshaping and fragmentation of NPs, there has not been a comprehensive study which takes into account the energy losses, the partial reshaping and fragmentation, the orientation, the size and the aspect ratio of NRs.

In this context, we propose to generalize the TM to determine the complete metastable phase diagram of gold NRs by taking into account convective and radiative losses. The absorption cross section of NRs is calculated by using the boundary element method (BEM)²⁵. Depending on the laser fluence and NR morphology, the NPs can be partially or fully melted and evaporated. This metastable phase diagram is used to predict the final shape distribution of NPs. The simulated distribution is in accordance with the shape distribution measured by transmission electron microscopy (TEM) after the laser

exposure. Although NRs are randomly oriented in colloidal suspensions, we show that the morphology of NR exposed to a ns laser pulse is mainly governed by the polarization parallel to the axis of NRs. We also explore the opportunity to tune the morphology of a broad NR shape distribution by selecting the adequate laser fluence.

Experimental

Three colloidal suspensions (S_1 , S_2 and S_3) which consist in Au NPs dispersed in water, are investigated. Their extinction spectra are reported in supplementary information (Fig. S1). S_1 and S_2 are purchased from Sigma Aldrich. S_3 is made according to the so-called seed-mediated growth method²⁶. First, a seed solution is synthesized by mixing 5 ml of an aqueous solution containing 5×10^{-4} M of HAuCl_4 and 0.2 M of CTAB with 0.6 ml of ice-cold 0.01 M NaBH_4 . Then, S_3 is obtained by mixing 0.25 ml of a solution containing 4×10^{-3} M AgNO_3 and 0.2 M CTAB, 70 μl of 0.08 M ascorbic acid, 5.0 ml of 0.001 M HAuCl_4 and 12 μl of the seed solution.

Transmission electron microscopy (TEM) analysis were performed with a Phillips CM200 TEM operated at 200 kV. The TEM grids were prepared by evaporating a drop of colloidal NP suspension on a copper TEM grid.

To investigate the laser-NP interaction, 1-2 ml of colloids introduced in a 1 cm light-path quartz cell is horizontally irradiated during 30 min with the fundamental wavelength (1064 nm) of a Nd-YAG laser (Continuum Surelite I). Longer exposure does not change the absorption spectra of colloids and so the NP shape and size distributions. During the exposure, the solution is continuously stirred with a magnetic stirrer. The maximum energy delivered by the laser is 400 mJ/pulse. The pulse width and the repetition rate are 6 ns and 10 Hz, respectively. The spatial profile of the output beam was reshaped by means of an intracavity apodizer in order to attenuate the hot spots inherent to the elliptical pumping configuration of the laser rod. The laser beam diameter is 4 mm. The laser fluence is controlled by changing the Q-switch delay.

Model

The laser-NR interaction in ns-pulse regime is related to a photothermal mechanism. Depending on the laser fluence, the energy absorbed by the NR could induce a rise of its temperature, its melting or its vaporization. In this context, we develop a modified Takami model (MTM) to describe the phase transitions induced by the absorption of laser pulses by NRs.

First, the absorption cross section of Au NRs in water is calculated at the 1064 nm laser wavelength by using the boundary element method (BEM)²⁵. BEM requires to define the interface between the NP core and the surrounding medium. The NR is considered as a cylinder capped by two hemispheres. Each NR is characterized by its minimum (d) and maximum (D)

Feret diameters and its aspect ratio ($r=d/D$). The dielectric function of Au and water are extracted from the Palik handbook²⁷. According to its symmetry, Au NRs support two plasmon resonances: the transversal (T-SPR) and the longitudinal plasmon modes (L-SPR) which can be selectively excited with a light polarized along the minor and major axes of NRs, respectively. Thus, we calculate the absorption cross section (σ_{L-SPR} , σ_{T-SPR}) for these two eigen polarization states. Then, the absorption cross section $\sigma(\theta, \varphi)$ for any NR orientations is deduced from the following equation:

$$\sigma(\theta, \varphi) = \sigma_{L-SPR} \sin^2(\varphi) \cos^2(\theta) + \sigma_{T-SPR} (\sin^2(\varphi) \sin^2(\theta) + \cos^2(\varphi)). \quad (1)$$

The angles θ and φ give the orientation of NR with respect to the incident polarization as illustrated in Fig. 1a.

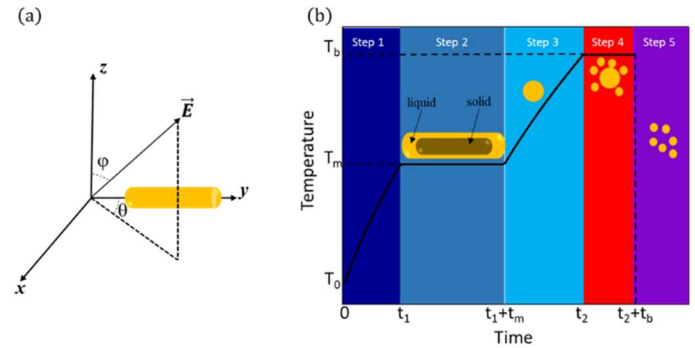


Fig. 1 (a) Definition of the orientation angles θ and φ of a single NR with respect to the incident polarization of the laser beam. (b) Typical evolution of the NR temperature and shape during the laser pulse.

Then, we numerically calculate the evolution of the NP temperature (T) during the laser pulse by using the energy conservation principle. As illustrated in Fig. 1b, this evolution occurs in several steps. During the step 1 ($0 < t < t_1$), the absorbed energy induces a rise of the NP temperature, without any change of the NP size and morphology. The evolution of the NP temperature is described by the following equation:

$$\rho_s \frac{\pi d^3}{12} \left(\frac{3}{r} - 1 \right) C_s \frac{dT}{dt} + \pi d \kappa (T - T_0) + \delta \frac{\pi d^2}{r} T^4 = \frac{\sigma F}{\tau} \text{ for } T < T_m. \quad (2)$$

The first term of equation (2) represents the heat of NR while the second and the third terms denote the convective and the radiative losses, respectively. The last term of equation (2) describes the absorbed light energy. $\rho_s = 19.32 \text{ g.cm}^{-3}$ and $C_s = 0.129 \text{ J.g}^{-1}.\text{K}^{-1}$ are the density and the heat capacity of Au in the solid state, respectively. $T_0 = 298 \text{ K}$ is the temperature of the solvent. $\tau = 6 \text{ ns}$ and $\delta = 5.67 \cdot 10^{-8} \text{ W.m}^{-2}.\text{K}^{-4}$ are the pulse width and the Stefan-Boltzmann constant, respectively. Due to the release of energy from NP to its environment, a thin layer of water vapor is formed around the NP²⁸. This layer acts as a thermal shield which limits the dissipation of energy by

convective losses. To take into account this effect, the thermal conductivity water vapor $\kappa = 0.0239 \text{ W.m}^{-1}\text{.K}^{-1}$ at 373 K²⁹ is used in equation (2). As suggested by Baffou *et al.*³⁰, the water bubble is generated at 550 K, i.e. at the spinodal temperature of water vapor. However, we check that the variations of κ between 373 K and 550 K are too small to have a significant impact on the metastable phase diagram of NPs.

The step 2 ($t_1 < t < t_1 + t_m$) starts when the NP temperature reaches the melting temperature $T_m = 1337 \text{ K}$ of Au. During this step, the NP temperature remains constant ($T=T_m$) and the absorbed energy only produces a phase transition of NP from the solid state to the liquid state. According to several authors²⁴, the melting starts from the NR surface. In other words, a liquid layer is formed around the crystalline core, suggesting that the NR is partially reshaped in surface. The complete melting of NP occurs during a time-lapse t_m given by:

$$t_m = \frac{\rho_s \frac{\pi d^3}{12} \left(\frac{3}{r} - 1\right) \Delta H_m}{\frac{\sigma F}{\tau} - \pi d \kappa (T_m - T_0) - \delta \frac{\pi d^2}{r} T_m^4}, \quad (3)$$

where $\Delta H_m = 67 \text{ J.g}^{-1}$ the heat of fusion of Au. After this time-lapse, the NP is completely melted and becomes spherical to minimize its surface energy. The diameter (d_l) of the resulted spherical NP is obtained by assuming an isochoric NP transformation:

$$d_l = d \left(0.5 \left(\frac{3}{r} - 1 \right) \right)^{1/3}. \quad (4)$$

During the step 3 ($t_1 + t_m < t < t_2$), the temperature of NP increases until it reaches the boiling temperature of Au ($T_b=3129 \text{ K}$) according to the following equation:

$$\rho_l \frac{\pi d^3}{12} \left(\frac{3}{r} - 1\right) C_l \frac{dT}{dt} + \pi d \kappa (T - T_0) + \delta \frac{\pi d^2}{r} T^4 = \frac{\sigma F}{\tau} \text{ for } T_m < T < T_b, \quad (5)$$

where $\rho_l=17.31 \text{ g.cm}^{-3}$ and $C_l=0.15 \text{ J.g}^{-1}\text{K}^{-1}$ the density and the heat capacity of Au in the liquid state. During the step 4 ($t_2 < t < t_2 + t_b$), the temperature of NP remains constant ($T = T_b$) and the absorbed energy is used to vaporize the NPs. This step occurs during a time-lapse (t_b) given by:

$$t_b = \frac{\rho_l \frac{\pi d^3}{12} \left(\frac{3}{r} - 1\right) \Delta H_b}{\frac{\sigma F}{\tau} - \pi d \kappa (T_b - T_0) - \delta \frac{\pi d^2}{r} T_b^4}, \quad (6)$$

where $\Delta H_b = 1578 \text{ J.g}^{-1}$ the heat of vaporization of Au. During this step, the NPs is partially fragmented. The evaporation occurs from the NP surface. If $\tau < t_2 + t_b$, the partial fragmentation produced both small clusters and a spherical NP core whose diameter is given by :

$$d_c = \left(\frac{6}{\pi} (t_2 + t_b - \tau) \frac{\frac{\sigma F}{\tau} - \pi d \kappa (T_b - T_0) - \delta \frac{\pi d^2}{r} T_b^4}{\rho_l \Delta H_b} \right)^{1/3}. \quad (7)$$

If $\tau \geq t_2 + t_b$ the NPs is entirely fragmented.

To summarize, depending on the pulse width $\tau = 6 \text{ ns}$, the NR can be:

- Unmodified if $\tau \leq t_1$
- Partially reshaped in surface if $t_1 \leq \tau \leq t_1 + t_m$
- Completely reshaped into spherical NP if $t_1 + t_m \leq \tau \leq t_2$
- Partially fragmented if $t_2 \leq \tau \leq t_2 + t_b$. The partial fragmentation produces clusters and a spherical NP with a diameter d_c
- Completely fragmented if $t_2 + t_b \leq \tau$. The fragmentation produces clusters.

The clusters generated during the NP fragmentation nucleate together to form primary NPs whose critical diameter (d_1) is determined by minimizing of the free energy of the NPs³¹:

$$d_1 = \frac{4\gamma \rho_l T_m}{\Delta H_m (T_m - T_0)}. \quad (8)$$

$\gamma = 0.27 \text{ N.m}^{-1}$ is the effective surface tension between melted gold and water. Primary NPs can be considered as monomers which coalesce each other to form secondary spherical NPs distributed in size. The evolution of the concentration n_k of secondary spherical NPs, resulted from the coalescence of k monomers, is given by³²:

$$\frac{dn_k}{dt} = \sum_{i+j=k} C_{ij} n_i n_j - \sum_{i \leq j} C_{ik} n_i n_k, \quad (9)$$

The diameter d_k of these secondary NPs is given by:

$$d_k = k^{1/3} d_1. \quad (10)$$

The first term on the right-hand side of equation (9) is the growth rate of NPs which have a diameter d_k while the second term is the rate at which they disappear to form larger NPs. The collision rate C_{ij} between NPs, calculated by considering a diffusion controlled coalescence process in the framework of rigid sphere approximation, are given by Itina³².

- Au NP has the same thermodynamic properties as bulk gold. This assumption is still valid for Au NP size higher than 5 nm ³³. In addition, according to the Biot parameter of NRs, which is in the 10^{-3} - 10^{-4} range³⁴, there is no gradient of temperature inside NRs.

-The thermodynamic constants are independent of the temperature. We only take into account the effect of phase transition on their value.

- The absorption cross section of NRs is constant during the NP phase transition. In other words, we don't take into account the variations of the absorption cross section of NRs during their reshaping and fragmentation.

- The variation of the dielectric function of Au with the temperature is neglected. Indeed, as shown by Miller³⁵, the melting of Au induces small variations of its dielectric function.

- The temperature of the solvent remains constant and equals to the ambient temperature during the laser exposure. Indeed, water is transparent at the laser wavelength (1064 nm). In addition, the concentration of NRs, which can be viewed as nanoheaters, is sufficiently small to neglect their impact on the temperature of the solvent. Thus, the solvent can be considered as a thermostatic medium.

- Rudnitzki *et al.*³⁶, show that the formation of bubble around the NPs induces a strong variation of their absorption cross section at the plasmon resonance. Indeed, due to the formation of a water vapor layer, the dielectric function around the NPs decreases and their plasmon resonance is blue shifted. To avoid this problem, we decide to use an off resonance laser wavelength. Indeed, the variation of the absorption cross section of NP is less pronounced at 1064 nm i.e. far from the plasmon resonance of the NP.

- The intensity of the laser beam is uniform in the colloidal suspension. This condition is obtained by using a laser equipped with an apodizer to avoid hot spots in the cross section of the laser beam. In addition, to minimize the attenuation of the laser beam in the solution, we deliberately use the fundamental wavelength of the Nd:YAG laser which is detuned from the plasmon resonance Au NRs.

- The laser dose is constant during the pulse. This latter is given by the ratio between the laser fluence and the laser pulse width. More realistic temporal laser profile can be considered, although it requires more computing resources. In addition, as we will show below, a pulse with a constant laser dose is enough to sketch the evolution of NR shape and to reproduce all experimental data.

- There is no cumulative effect induced by multipulse absorption. After the laser pulse, the NP cool down until its temperature reaches the room temperature. By vanishing the source term in the MTM model, we estimate that this cooling process occurs within few μs which is less than the considered pulse-to-pulse interval.

-The orientation of NRs does not change during the laser pulse. Indeed, by modeling the NR as a cylinder, its angular velocity (ω) can be estimated from statistical physics by using the following equation:

$$\omega = \sqrt{\frac{192 r^3 k_0 T}{\rho \pi d^5 (3r^2 + 4)}}, \quad (11)$$

where k_0 is the Boltzmann constant. To give an order of magnitude of the angular velocity, we consider a NR which have a minimal Feret diameter of 10 nm and aspect ratio of 0.2. This NR is maintained at $T=1000$ K. The angular velocity of this NR is estimated to $3 \times 10^7 \text{ rad.s}^{-1}$. As a consequence, this NR is turned through 10° during 6 ns, confirming that we can neglect the rotation of NR during the laser pulse.

Results and discussion

Effect of the laser fluence

To explore the effect of the laser fluence on the NP morphology, two suspensions (S_1 and S_2) are exposed to the laser beam. Several laser fluences are investigated: 3.2 J.cm^{-2} , 0.8 J.cm^{-2} and 0.4 J.cm^{-2} for S_1 and 1.6 J.cm^{-2} , 0.8 J.cm^{-2} for S_2 . These suspensions are named $S_{1,F}$ and $S_{2,F}$, where F is the laser fluence. TEM images (Fig. 2) reveal that the initial S_1 and S_2 suspensions are composed of NRs with narrow shape distributions. The mean values of aspect ratio and minimum Feret diameter of S_2 NRs are 0.6 and 27 nm, respectively. On the other hand, S_1 NRs exhibit a more pronounced anisotropy. Their mean aspect ratio and minimum Feret diameter are 0.28 and 8 nm, respectively. The exposure of S_1 and S_2 NRs to the laser beam leads to NP morphology transformation (Fig. 2). $S_{1,3.2}$ is composed of nearly spherical NPs which have a minimum Feret diameter smaller than 10 nm. This population of NPs, named P1, is also observed in $S_{1,0.8}$, $S_{1,0.4}$, and $S_{2,1.6}$. However, there are accompanied with another population of NPs (P2) which consists in nearly spherical NPs with a 15-20 nm minimum Feret diameter. This bimodal NP size distribution has been previously reported by several authors^{14,37}. In addition, a large amount ϕ -shaped NPs are also clearly observed in the TEM images of $S_{1,0.4}$ (Fig. 3b). Such NPs have been previously reported by Link *et al.*^{2,38}. The second population of $S_{2,1.6}$ NPs is composed of nearly spherical NPs which have a 25 nm mean diameter. $S_{2,0.8}$ NRs aspect ratio and size are similar to those of S_2 . However, S_2 NRs are faceted while $S_{2,0.8}$ NRs exhibits smooth edges (Fig. 3c-d). In addition, $S_{2,0.8}$ contains a larger amount of nearly spherical NPs than S_2 , which have a 20-45 nm diameter.

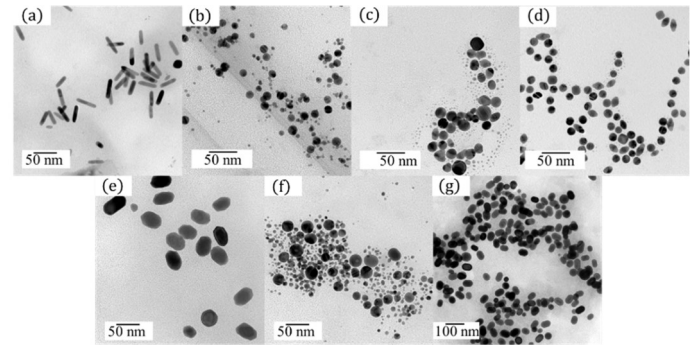


Fig. 2 TEM images of (a) S_1 , (b) $S_{1,3.2}$, (c) $S_{1,0.8}$, (d) $S_{1,0.4}$, (e) S_2 , (f) $S_{2,1.6}$ and (g) $S_{2,0.8}$ NPs.

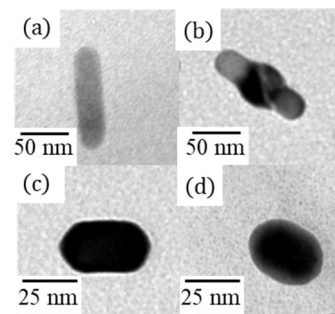


Fig. 3 TEM images of (a) S_1 , (b) $S_{1,0.4}$, (c) S_2 , (d) $S_{2,0.8}$ NPs.

To interpret the evolution of NP shape during the laser exposure, we simulate the metastable phase diagram of NRs by using the MTM model. These simulations are performed for incident light polarized along the major axes of NRs. The metastable phase diagram is calculated in a 2-dimensional space (r , d). In this space, each NR is represented by a unique point whose coordinates correspond to its aspect ratio and minimum Feret diameter. As shown in Figure 4, five loci can be distinguished on metastable phase diagrams. As expected, the locus of unmodified NPs is dominant for small spherical NPs and low laser fluence. Indeed, the absorption cross section of NPs increase with the NPs diameter³⁹. In addition, the laser wavelength is far from the plasmon band of spherical NPs located at 530 nm⁴⁰. As a consequence, small spherical NPs have a weak interaction with the laser beam. Moreover, the ratio between convective or radiation losses and the heat energy increases with the surface to volume ratio. Indeed, as shown in Figure S2, these losses as a strong impact for NPs which have a minimum Feret diameter smaller than 15 nm, confirming that small spherical NPs exhibit high convective and radiative losses. The NR metastable phase diagram evolves gradually towards the complete fragmentation as the NR aspect ratio decreases. Indeed, a decrease of the NR aspect ratio induces a redshift of its longitudinal plasmon band and a rise of

(equation (8)). These primary NPs coalesce each other to form secondary spherical NPs whose diameter is smaller than 10 nm as observed in $S_{1,3.2}$, $S_{1,0.8}$, $S_{1,0.4}$, and $S_{2,1.6}$. The second population (P2) of larger NPs in $S_{1,0.8}$, $S_{1,0.4}$, and $S_{2,1.6}$ can have two origins: the partial fragmentation and the complete reshaping of NPs. Indeed, at the 0.8 J.cm⁻² and 0.4 J.cm⁻² laser fluences, some S1 NRs are located in the partial fragmentation and the complete reshaping domains of the metastable phase diagram simulated for a 1.6 J.cm⁻² fluence. The partial fragmentation generates spherical NP cores whose diameters are given by equation (7). The diameter of the core NPs in $S_{1,0.8}$ and $S_{1,0.4}$ is in the 10-15 nm range while the $S_{2,1.6}$ one is in the 20-35 nm range. These NP sizes are in agreements with the ones measured by TEM. In addition, at 1.6 J.cm⁻² and 0.8 J.cm⁻² fluences, S2 NRs are also reshaped and become spherical. Their mean diameter determined from equation (4), is 30 nm. This reshaping process explained the rise of the amount of spherical NPs in $S_{2,0.8}$. Moreover, some S2 NPs are also located in the partial reshaping domains of the metastable phase diagram simulated at 0.8 J.cm⁻². Their surface is melted and reconstructed. Thus, the NP facets disappear without any change of their size and aspect ratio (Fig. 3).

As observed in $S_{1,0.4}$ (Fig. 3), the interaction of highly anisotropic

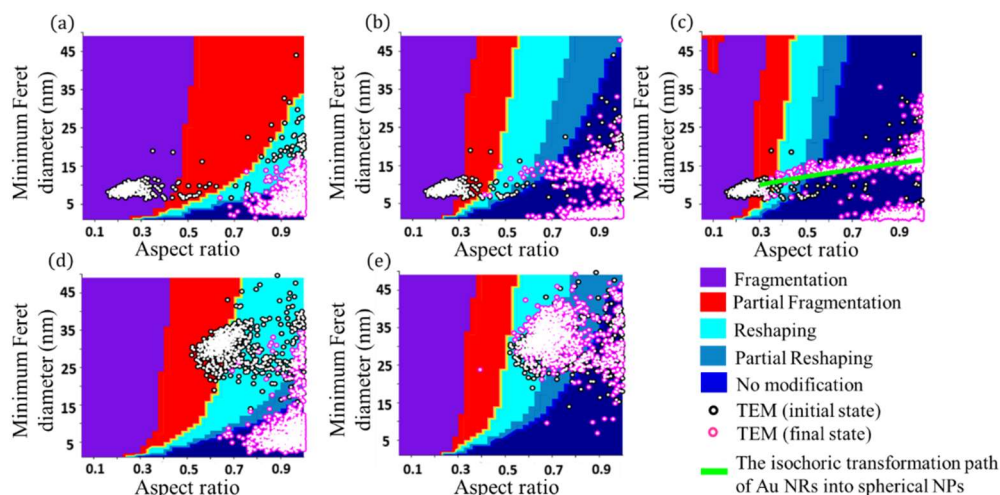


Fig. 4 Metastable Phase diagrams in the (d , r) space of Au NRs calculated at (a) 3.2, (d) 1.6, (b)(e) 0.8 and (c) 0.4 J.cm⁻² laser fluences. Each NP observed by TEM for (a) $S_{1,3.2}$, (b) $S_{1,0.8}$, (c) $S_{1,0.4}$, (d) $S_{2,1.6}$ and (e) $S_{2,0.8}$ are represented as pink dot. The raw NPs observed in (a)(b)(c) S_1 and (d)(e) S_2 NPs are also represented by black dots. The green solid line in (c) is the isochoric transformation path of Au NRs into spherical NPs.

the NR absorption cross section at the excitation wavelength⁴⁰.

Each NP observed by TEM before and after the laser exposure are reported on the metastable phase diagrams (Fig. 4). This representation is used to explain the evolution of the NP morphology during the laser exposure. After the laser exposure, NPs are mainly localized in the unmodified NPs or partial reshaping domains of metastable phase diagrams. The population P1 of small spherical NPs, is only observed when the initial distribution of S1 or S2 NRs are located in the locus of partial or complete fragmentation. Indeed, these processes produce to primary NPs whose diameter is estimated at 0.8 nm

NRs with low fluence nanosecond pulses promotes the formation of ϕ -shaped NPs^{2,38}. Their aspect ratio and minimum Feret diameter are in the 0.5-0.8 and 12 nm-17 nm ranges, respectively. At 0.4 J.cm⁻², some S2 NRs are located in the partial fragmentation domain. According to the MTM model, the NR surface is evaporated while the core is in liquid state. As a consequence, the NP core is transformed into the more thermodynamically favored spherical shape. We simulate the evolution of the NPs shape during the reshaping process. By neglecting the evaporation process which occurs on the NP surface, the NP undergoes an isochoric transformation. This assumption is valid, since the thickness of the evaporated layer

of S_1 NRs, estimated from the MTM model, is smaller than 1 nm at 0.4 J.cm^{-2} . During the reshaping process, the minimum Feret diameter (d) and the aspect ratio (r) of NRs must respect the following relation:

$$d = d_0 \left(\frac{r^3 - r_0}{r_0^3 - r} \right)^{\frac{1}{3}}, r_0 < r \leq 1, \quad (12)$$

with d_0 and r_0 the initial minimum Feret diameter and aspect ratio of NRs. As shown in Figure 3e, $S_{1,0.4}$ ϕ -shaped NPs are located on the reshaping path defined by equations (12), confirming that these NPs result from the NR reshaping process. If the NP core cools off faster than the reshaping process, it returns to its solid state before it reaches the spherical shape. The shape of the resulted NPs, which are located in the unmodified NPs area of the metastable phase diagram, remains unaffected by successive pulses.

To summarize, we can distinguish three laser fluence regimes. At high fluence, NRs are completely fragmented into small and nearly spherical NPs. At intermediate fluence, the competition between the fragmentation and reshaping processes leads to a bimodal distribution of NPs. The low fluence regime is governed by the partial and complete reshaping processes. NPs have smooth edges and tend to be more spherical. For highly anisotropic NPs, the competition between the cooling and the reshaping processes produced f-shaped NPs. Despite NRs are randomly oriented in suspension, metastable phase diagrams simulated for light polarized along the major axis of NR allows explaining the NP distributions obtained after the laser exposure. By considering the spectral range of L-SPR mode, the highest absorption cross section of NRs at 1064 nm is obtained when this mode is selectively excited. In other words, the absorption cross section is minimized and the NR remains almost unchanged when the incident light is polarized along its minor axis. Due to its random movement, this NR can be realigned during the successive pulses. We conclude that, due to the multi-pulse exposure, σ_{L-SPR} plays a key role to determine the minimum fluence threshold of the fragmentation and reshaping processes (see supplementary information).

Application of the MTM model: Control and prediction of the NP shape distribution

Figure 5 shows the TEM image of S_3 NRs. The minimal Feret diameter and aspect ratio of each NR observed by TEM is also reported in Figure 6. S_3 is composed of Au NRs which exhibit a broad shape and size distributions. Their aspect ratio and minimum Feret diameter are in the 0.2-1 and 3-25 nm ranges, respectively. This kind of distribution is often obtained by chemical synthesis route. NR distribution refinement can be achieved by time consuming post-synthesis treatment such as density gradient ultracentrifugation⁴¹. As reported by several authors^{2, 4, 14}, photothermal effect can be considered as an alternative to tune the NR size and shape distributions. However, the choice of the adequate laser fluence is crucial issue to design the NR distribution. In this context, we propose

to exploit the MTM model to correlate the fluence to the distribution achieved after the exposure.

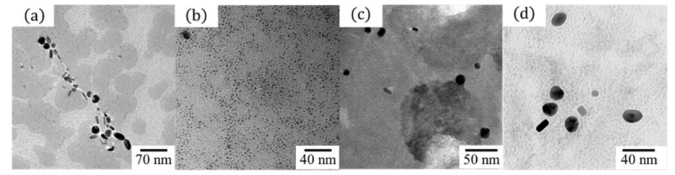


Fig. 5 TEM images of S_3 NRs (a) before and after 30 min of laser exposure at (b) 1.6 J.cm^{-2} , (c) 0.8 J.cm^{-2} and (d) 0.4 J.cm^{-2} laser fluences.

To refine their distribution, S_3 NRs are exposed to 3 laser fluences ($F=1.6 \text{ J.cm}^{-2}$, 0.8 J.cm^{-2} and 0.4 J.cm^{-2}) during 30 min. Figures 5 and 6 show the TEM images and the distribution of S_3 NRs obtained after laser exposure. As expected, the width of the NR distributions decreases as the laser fluence increases. Indeed, at $F=0.4 \text{ J.cm}^{-2}$, only the NRs which have an aspect ratio smaller than 0.4 are suppressed, while at the higher fluence, the suspension is mainly composed of nearly spherical NPs.

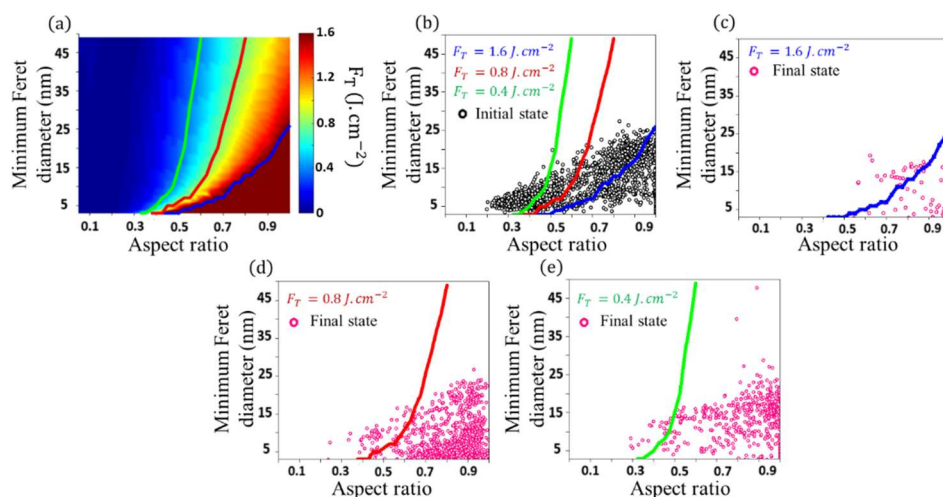


Fig. 6 (a) Laser fluence threshold F_T of NRs, simulated in the (d,r) space by the MTM model. Representation in the (d,r) space of S3 NRs observed by TEM before (black dots) and after the laser exposure (pink dots) at (b) 1.6 J.cm^{-2} , (c) 0.8 J.cm^{-2} and (e) 0.4 J.cm^{-2} . The green, red and blue lines correspond to the loci of $F_T=1.6 \text{ J.cm}^{-2}$, 0.8 J.cm^{-2} and 0.4 J.cm^{-2} , respectively.

As reported in the previous section, fragmentation and complete reshaping processes allow suppressing some NRs of raw suspension. As complete reshaping occurs at a smaller laser fluence than the complete fragmentation, the laser fluence threshold F_T , defined as the minimal fluence required for complete NP reshaping, is a crucial parameter to control the NP distributions. Figure 6 correlates the fluence threshold F_T determined from the MTM model to the aspect ratio and minimum Feret diameter of NRs. The fluence threshold decreases as the minimum Feret diameter of NRs increases. In addition, its value is reduced for highly anisotropic NRs. This behavior is in accordance with the variation of absorption cross section of NRs at 1064 nm with their size and aspect ratio. As a consequence, we expect that photothermal effect can be used to reduce the width of NR distribution by suppressing the larger and the more anisotropic NRs. This conclusion is in agreement with TEM images performed on exposed S3 NRs (Fig. 5). As shown in Figure 6, for each laser fluence F , we can define in the (r,d) space two domains separated by the loci defined by $F_T=F$. In accordance with the MTM model, we remark that the NRs are suppressed if their fluence threshold is smaller than the laser fluence ($F_T \leq F$) (Fig. 6). Thus, MTM model can be used to finely define the laser fluence required to obtain the desired NP distribution.

We want to push the limit of the MTM model toward the prediction of the NR distributions obtained after the laser exposure, by adopting the following procedure. For each NR observed in TEM, two orientation angles (θ, φ) are randomly generated. Then, we applied the MTM model on these NRs to determine the size and shape of daughter NPs obtained after the first laser pulse. Due to the NP fragmentation process, the number of NPs increases during the computation. However, the MTM model insures the conservation of the total volume occupied by NPs. The same procedure is then repeated on daughter NPs to simulate multipulse exposure. This procedure is run until the distribution of daughter NPs converges. Figure 7 compares the distribution of S3 NRs measured by TEM to the simulated ones by MTM model. The MTM model reproduces all distributions observed by TEM. This result suggests that the MTM model is a powerful tool to predict the NR distribution obtained after the laser exposure.

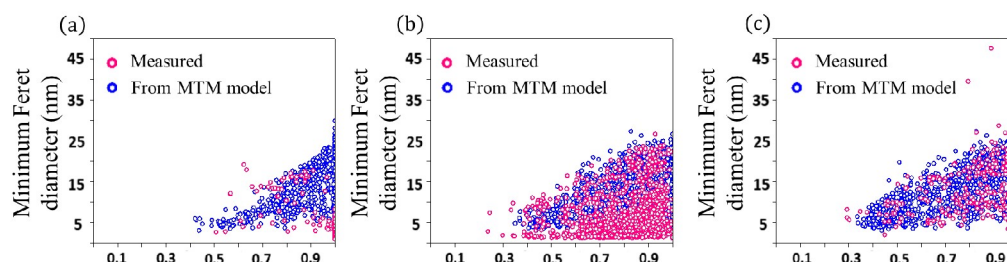


Fig. 7 Measured (pink dots) and simulated (blue dots) NR distribution after the exposure of S3 to (a) 1.6 J.cm^{-2} , (b) 0.8 J.cm^{-2} and (c) 0.4 J.cm^{-2} laser fluences.

Conclusion

In summary, we have introduced a modified Takami model (MTM) to describe the photothermal effect which occurs during the interaction between Au NRs and ns-laser pulse. This model takes into account the orientation of NR, the radiative and convective losses, and the phase transitions of NRs. The MTM is used to simulate the evolution of temperature and the shape and size transformation of NRs during the laser exposure. By analyzing TEM measurements with the MTM model, we shown that the NP shape is governed by the fragmentation and reshaping processes. At high laser fluence, the complete fragmentation leads to a population of nearly spherical NPs while at moderate laser fluence, the partial fragmentation and reshaping processes generates a bimodal distribution. Due to competition of cooling and reshaping processes, highly anisotropic NRs are transformed into ϕ -shape NPs at low laser fluence. By calculating the fluence threshold F_T , we also shown that the MTM model can be used to determine the laser fluence required to suppress some specific NRs shapes. By simulating the evolution of the shape the NP initially observed by TEM, we predict, for the first time, to our knowledge, the NP size and shape distributions obtained after the laser exposure. Thus, the MTM can be viewed as a powerful tool to investigate the interaction between NR and ns-pulse.

Conflicts of interest

There are no conflicts to declare.

Notes and references

- 1 A. Poletti, G. Fracasso, G. Conti, R. Pilota and V. Amendola, *Nanoscale*, 2000, **7**, 13702-13714.
- 2 S. Link, C. Burda, B. Nikoobakht and M. A. El-Sayed, *J. Phys. Chem. B*, 2000, **104**, 6152-6163.
- 3 F. Mafune, J.-Y. Kohno, Y. Takeda and T. Kondow, *J. Phys. Chem. B*, 2003, **107**, 12589-12596.
- 4 F. Mafune, J.-Y. Kohno, Y. Takeda and T. Kondow, *J. Phys. Chem. B*, 2002, **106**, 7575-7577.
- 5 R. E. Cavicchi, D. C. Meier, C. Presser, V. M. Prabhu and S. Guha, *J. Phys. Chem. C*, **117**, 2013, 10866-10875.
- 6 Y. A. Attia, M. T. Flores-Arias, D. Nieto, C. Vázquez-Vázquez, G. F. De La Fuente and M. A. López-Quintela, *J. Phys. Chem. C*, 2015, **119**, 13343-13349.
- 7 T.-H. Park and D.-J. Jang, *Nanoscale*, 2018, **10**, 20108.
- 8 O. Ekici, R. K. Harrison, N. J. Durr, D. S. Eversole, M. Lee and A. Ben-Yakar, *J. Phys. D: Appl. Phys.*, 2008, **41**, 185501.
- 9 R. R. Letfullin, C. Joenathan, T. F. George and V. P. Zharov, *Nanomedicine*, 2006, **1**, 473-480.
- 10 V. K. Pustovalov, A. S. Smetannikov and V. P. Zharov, *Laser Phys. Lett.*, 2008, **5**, 775-792.
- 11 V. P. Zharov, E. N. Galitovskaya, C. Johnson and T. Kelly, *Lasers in Surgery and Medicine*, 2005, **37**, 219-226.
- 12 J. Morales-Dalmau, C. Vilches, I. de Miguel, V. Sanza and R. Quidant, *Nanoscale*, 2018, **10**, 2632.
- 13 D. Werner, T. Ueki and S. Hashimoto, *J. Phys. Chem. C*, 2012, **116**, 5482-5491.
- 14 D. Werner and S. Hashimoto, *Langmuir*, 2013, **29**, 1295-1302.
- 15 S.-S. Chang, C.-W. Shih, C.-D. Chen, W.-C. Lai and C. R. C. Wang, *Langmuir*, 1999, **15**, 701-709.
- 16 D. Werner and S. Hashimoto, *J. Phys. Chem. C*, 2011, **115**, 5063-5072, 2011.
- 17 A. Plech, S. Ibrahimkutti, S. Reich and G. Newby, *Nanoscale*, 2017, **9**, 17284.
- 18 A. Pyatenko, M. Yamaguchi and M. Suzuki, *J. Phys. Chem. C*, 2009, **113**, 9078-9085.
- 19 D. Werner, A. Furube, T. Okamoto and S. Hashimoto, *J. Phys. Chem. C*, 2011, **115**, 8503-8512.
- 20 A. Pyatenko, H. Wang, N. Koshizaki and T. Tsuji, *Laser Photonics Rev.*, 2013, **7**, 596-604.
- 21 A. Takami, H. Kurita and S. Koda, *J. Phys. Chem. B*, 1999, **103**, 1226-1232.
- 22 T. S. Ahmadi, S. L. Logunov, and M. A. El-Sayed, *J. Phys. Chem.*, 1996, **100**, 8053-8056.
- 23 G. V. Hartland, Optical studies of dynamics in noble metal nanostructures, *Chem. Rev.*, 111, 3858-3887, 2011.
- 24 S. Inasawa, M. Sugiyama and Y. Yamaguchi, *J. Phys. Chem. B*, 2005, **109**, 3104-3111.
- 25 U. Hohenester and A. Trügler, *Computer Physics Communications*, 2012, **183**, 370-381.
- 26 B. Nikoobakht and M. A. El-Sayed, *Chemistry of Materials*, 2003, **15**, 1957-1962.
- 27 E. D. Palik, Handbook of Optical Constants of Solids, Academic Press, Boston, 1998.
- 28 J. Lombard, T. Biben and S. Merabia, *Nanoscale*, 2016, **8**, 14870-14876.
- 29 R. C. Weast, CRC Handbook of chemistry and physics, Chemical Rubber co, Cleveland, 1969.
- 30 K. Metwally, S. Mensah and G. Baffou, *J. Phys. Chem. C*, 2015, **119**, 28586-28596.
- 31 J. Park, V. Privman and E. Matijevic, *J. Phys. Chem. B*, 2001, **105**, 11630-11635.
- 32 T. E. Itina, *J. Phys. Chem. C*, 2011, **115**, 5044-5048.
- 33 P. Buffat and J. P. Borel, *Physical review A*, 1976, **13**, 2287.
- 34 O. Ekici, R. K. Harrison, N. J. Durr, D. S. Eversole, M. Lee and A. Ben-Yakar, *J. Phys. D: Appl. Phys.*, 2008, **41**, 185501.
- 35 J. C. Miller, *Philosophical Magazine*, 1969, **20**, 1115-1132.
- 36 F. Rudnitzki, M. Bever, R. Rahmzadeh, K. Brieger, E. Endl, J. Groll and G. Hüttmann, *J. Biomed. Opt.*, 2012, **17**, 058003.
- 37 S. Inasawa, M. Sugiyama and Y. Yamaguchi, *J. Phys. Chem. B*, 2005, **109**, 9404-9410.
- 38 S. Link, Z. L. Wang and M. A. El-Sayed, *J. Phys. Chem. B*, 2000, **104**, 7867-7870.
- 39 Y. Battie, A. Resano-Garcia, N. Chaoui, Y. Zhang and A. En Naciri, *J. Chem. Phys.*, 2014, **140**, 044705.
- 40 A. Resano-Garcia, Y. Battie, A. En Naciri, S. Akil and N. Chaoui, *J. Chem. Phys.*, 2015, **142**, 134108.
- 41 S. Li, Z. Chang, J. Liu, L. Bai, L. Luo and X. Sun, *Nano Research*, 2011, **4**, 723-728.